Deep Indentation of Soft Thin Films Beyond the 10% Rule

Huang Lu and Zhaohe Dai*
School of Mechanics and Engineering Science, State Key Laboratory for Turbulence and Complex Systems, Peking University, Beijing 100871, China

(Received 19 November 2025; accepted 25 June 2026; published 14 July 2026)

Indentation is one of the simplest ways to feel the stiffness of matter. Interpreting indentation, however, requires care, especially for thin films—such as biological cells or soft coatings supported by rigid substrates—because the substrate effect can make a film appear orders of magnitude stiffer than it actually is. To minimize this artifact, the empirical "10% rule of thumb," which limits indentation depth to one-tenth of the film thickness, has often been adopted, though it becomes unreliable and impractical for ultrathin films. Here, we explore the traditionally forbidden regime: *deep indentation*, where the indentation depth is comparable to the film thickness. We develop an asymptotic theory that incorporates nonlinear geometry and elasticity, elucidating a simple indentation force-depth relation in this deep regime. We further show that the pull-off force in such indentation tests is remarkably independent of both the material law and geometric nonlinearity. The results provide a unified framework for interpreting thin-film mechanics under deep indentation, a regime that is generally much more accessible in experiments on very thin films.

DOI: 10.1103/8s5j-63xf

Poking is an instinctive way to assess the stiffness of an object [1–4]. For soft, thin objects such as a rubber band/sheet, this method is sensible when the sheet is held, and the poking is applied on the suspended region (just like poking a drumhead). The response, however, is dramatically different when the same sheet rests flat on a glass table: the support constrains deformation and makes the sheet appear much stiffer, especially for larger fingers or thinner sheets [5].

This simple observation captures the central dilemma in indentation experiments on thin coatings and biological cells that are usually supported by rigid substrates [6,7]. To mitigate the substrate-induced stiffening, experiments commonly employ sharp pyramidal tips ("very small fingers") and restrict the indentation depth to less than one-tenth of the film thickness—an empirical guideline known as the "10% rule of thumb" [8]. However, this rule is neither reliable nor practical for ultrathin films [8–10]. (i) Theoretical models underlying this rule typically assume linear elasticity, yet sharp indenters can induce local strains that exceed the linear regime and even damage the material [9,10]. (ii) Moreover, even a pyramidal tip has a finite radius of curvature R (typically tens of nanometers), so the lateral contact size scales as $\sqrt{R\delta}$, with δ being the indentation depth [11]. The substrate can then be clearly "felt" when $\sqrt{R\delta} \sim h$ even at $\delta \approx h/10$ if $R \gtrsim h$. (iii) Consequently, avoiding substrate effects in very thin films requires extremely shallow indentation ($\delta \ll h^2/R$), entering a regime where the true contact onset becomes uncertain due to long-range tip–sample interactions [12,13].

In this Letter, rather than confronting the difficulties inherent to shallow indentation, we explore a traditionally "forbidden" and unexplored regime: using large spherical tips to perform deep indentations beyond the 10% limit [Fig. 1(a)]. The advantages are immediate. Large spherical indenters are geometrically well defined, mechanically robust, and free of local stress concentrations, while deep indentations generate sufficiently large forces that render the subtleties of establishing initial contact negligible. The primary challenge instead lies in developing a model capable of capturing the mechanical response of a substrate-confined thin film under strong geometric and material nonlinearities—a task that has remained elusive. Remarkably, we show that for this class of problems, the full three-dimensional nonlinear problem can be reduced to a simple algebraic relation, rendering the deep-indentation regime analytically tractable. Furthermore, once adhesion is established during indentation, we demonstrate that the force required to detach the indenter is strikingly independent of both material and geometric nonlinearities, providing a universal framework for probing adhesion in thin films.

As illustrated in Fig. 1(a), the problem concerns a rigid spherical indenter of radius R pressing into a thin elastic film of thickness $h \ll R$. In the contact region, the downward indentation displacement can be approximated by

$$w_s(r) \approx \delta - \frac{r^2}{2R}, \tag{1}$$

where δ is the indentation depth. The objective is to determine the relationship between the indentation depth

*Contact author: daizh@pku.edu.cn

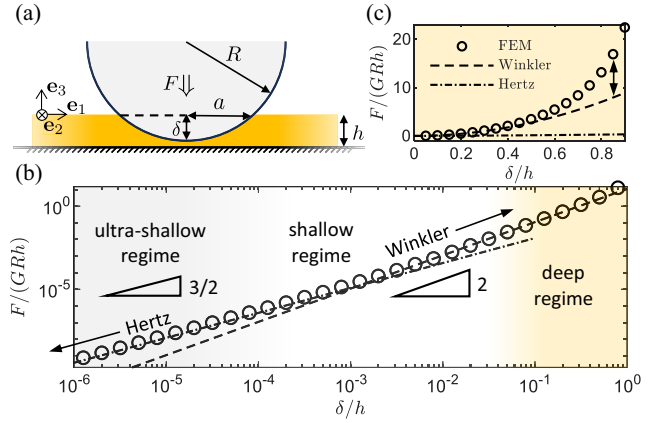

FIG. 1. (a) Schematic of large-sphere deep indentation: a rigid indenter of radius R subjected to indentation force F penetrates a soft film of thickness $h \ll R$ by a depth δ, generating a contact radius a. (b) Indentation regimes governed by δ/h: an *ultra-shallow* regime ($\delta/h \ll h/R$), where the substrate is not felt by the indenter and the Hertz solution applies; a *shallow* regime ($\delta/h \ll 1$), where the Winkler mattress model is a good approximation; and a *deep* regime ($\delta/h \sim O(1)$), which is most sensible in experiments on ultrathin films. (c) Force-displacement relation in the deep-indentation regime, where both Hertz and Winkler models significantly underestimate the force. Markers in (b), (c) show finite element method (FEM) results for a compressible neo-Hookean material with $R/h = 100$.

δ, the contact radius a, and the applied indentation force F for the elastic film. We start by considering the film as a compressible neo-Hookean material characterized by a strain-energy function [14]:

$$\Phi = \frac{G}{2}(\mathcal{I}_1/\mathcal{I}_3{}^{1/3} - 3) + \frac{G(1+\nu)}{3(1-2\nu)}(\mathcal{I}_3{}^{1/2} - 1)^2, \quad (2)$$

where $\mathcal{I}_1$ and $\mathcal{I}_3$ are the first and third principal invariants of the right Cauchy-Green tensor of the deformation, and G and ν are the shear modulus and the Poisson's ratio, respectively, in the infinitesimal linear elasticity limit. Unless otherwise stated, we use $h = 0.1$ mm, $R = 10$ mm, $G = 1$ MPa, and $\nu = 0.3$ for demonstration, and the corresponding finite element method (FEM) results for the indentation problem are shown in Figs. 1(b) and 1(c) (see Section I.A of [15]).

The horizontal length scale in this problem depends on both the indentation depth and the sphere radius ($\sqrt{R\delta}$) [18]. Consequently, the effective thickness of the film is governed by $h/\sqrt{R\delta}$. The classical Hertz solution,

$$F_{\text{Hertz}} = \frac{8}{3(1-\nu)} G R^{1/2} \delta^{3/2}, \quad (3)$$

which was developed for an elastic slab, is applicable only in the extremely shallow indentation regime ($\delta/h \ll h/R$) [Fig. 1(b)]. As the indentation depth increases, the influence of the underlying substrate becomes significant, requiring, in general, the solution of a mixed-boundary problem.

However, for ultrathin films, there exists an intermediate shallow regime in which the film is slender and the deformation remains small, i.e., $h^2/R \ll \delta \ll h$. In this regime, the mechanical response of the film can be approximated by a Winkler mattress model [i.e., an array of independent linear springs; Fig. 2(a)], characterized by a local pressure-displacement relation [16]:

$$p = \frac{2(1-\nu)G}{(1-2\nu)h} w_{\text{s}}. \quad (4)$$

Integration over the contact area yields the total load [19]:

$$F_{\text{Winkler}} = \frac{2\pi(1-\nu)GR}{(1-2\nu)h} \delta^2, \quad (5)$$

which reproduces the δ^2 scaling of the indentation force observed in the intermediate regime shown in Fig. 1(b).

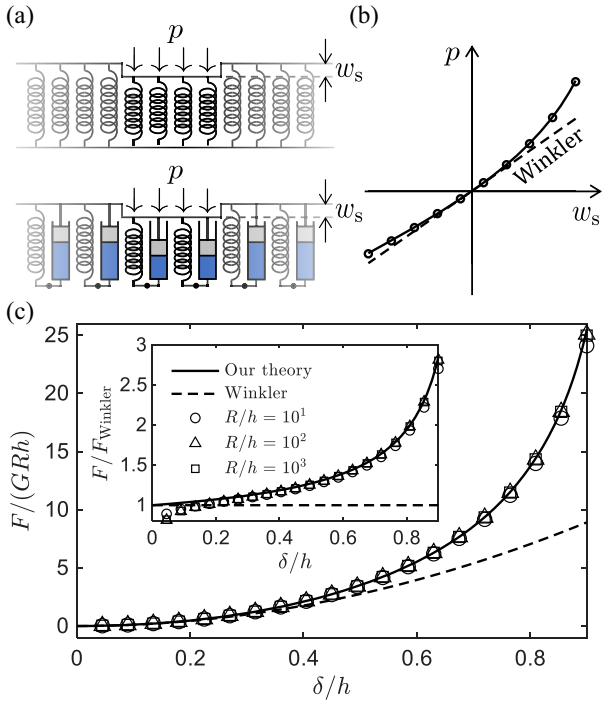

FIG. 2. (a) Schematic comparison between the classical Winkler foundation (an array of linear springs) and the present model (a gas-elastic spring system). (b) Nonlinear pressure-displacement relation exhibiting compression hardening and tension softening, in contrast to the linear Winkler response. Dashed and solid curves correspond to the Winkler model [Eq. (4)] and our nonlinear model [Eq. (11)], respectively; open circles denote the gas-elastic spring system [Eq. (12)]. (c) Indentation force-depth curves for different R/h, predicted by our nonlinear model in Eq. (14) (solid curves) and by the linear Winkler model in Eq. (5) (dashed curves), together with numerical results (circles).

The experimentally accessible indentation range can be substantially extended by relaxing the constraint $\delta \ll h$. However, in such deep indentation regimes, both the Hertz theory and the Winkler model underestimate the indentation force. This discrepancy is more clearly evident in an experimentally relevant linear-scale plot shown in Fig. 1(c). The numerical results begin to deviate from the Winkler model at approximately $\delta/h = 0.1$, marking the onset of geometric nonlinearity. It is worth noting that the effective slenderness of the film increases further in this regime, a feature that we exploit to develop a nonlinear model for deep indentation [20].

To describe the geometrical nonlinearities, we consider the finite deformation described by the mapping $\mathbf{x} = \chi(\mathbf{X})$ from the material point $\mathbf{X}$ in the reference configuration to the spatial point $\mathbf{x}$ in the current configuration, with displacement $\mathbf{u} = \mathbf{x} - \mathbf{X}$. The deformation gradient tensor is $\mathbf{F} = \mathbf{I} + \partial\mathbf{u}/\partial\mathbf{X}$, where $\mathbf{I}$ is an identity tensor. We establish Cartesian coordinates $\{O; \mathbf{e}_1, \mathbf{e}_2, \mathbf{e}_3\}$ in both configurations, with $\mathbf{e}_3$ pointing upward and $\mathbf{e}_1$, $\mathbf{e}_2$ lying in the plane. Without loss, we consider thin films with $h \ll \ell$ (where ℓ is some transverse characteristic length) and introduce the slenderness parameter $\epsilon = h/\ell \ll 1$. It is then natural to scale the components of material coordinates $\mathbf{X}$ and displacement $\mathbf{u}$ as $(\hat{\mathbf{X}}) = (\hat{X}, \hat{Y}, \hat{Z}) = (\epsilon X/h, \epsilon Y/h, Z/h)$ and $(\hat{\mathbf{u}}) = (\hat{u}, \hat{v}, \hat{w}) = (u/\epsilon h, v/\epsilon h, w/h)$. The deformation gradient tensor can then be rewritten as

$$\mathbf{F} = (\mathbf{I} + \hat{w}_{\hat{Z}}\mathbf{e}_3 \otimes \mathbf{e}_3) + \epsilon(\hat{w}_{\hat{X}}\mathbf{e}_3 \otimes \mathbf{e}_1 + \hat{w}_{\hat{Y}}\mathbf{e}_3 \otimes \mathbf{e}_2 + \hat{u}_{\hat{Z}}\mathbf{e}_1 \otimes \mathbf{e}_3 + \hat{v}_{\hat{Z}}\mathbf{e}_2 \otimes \mathbf{e}_3) + \mathcal{O}(\epsilon^2), \tag{6}$$

where the subscripts denote partial derivatives with respect to the corresponding coordinates. Note that starting from Eq. (6), we only summarize the asymptotic calculations here; the full derivations are provided in Section II.C of [15].

Interestingly, to leading order, the deformation gradient $\mathbf{F}$ depends solely on the through-thickness gradient of the vertical displacement, $\hat{w}_{\hat{Z}}$. This implies that, similar to the Winkler model, the local pressure is governed exclusively by the local deformation, even when geometric nonlinearity is taken into account. Consequently, for a general strain-energy function, we may express the following asymptotic expansion:

$$\Phi(\mathbf{F}) = \Phi^{(0)}(\hat{w}_{\hat{Z}}) + \epsilon\Phi^{(1)}(\hat{w}_{\hat{Z}}, \hat{w}_{\hat{X}}, \hat{w}_{\hat{Y}}, \hat{u}_{\hat{Z}}, \hat{v}_{\hat{Z}}) + \mathcal{O}(\epsilon^2). \tag{7}$$

As such, the first Piola-Kirchhoff stress can be given by $\mathbf{P} = \partial\Phi/\partial\mathbf{F}$, which, together with the leading-order equilibrium equation at $\mathbf{e}_3$ direction, leads to simply

$$\hat{w}_{\hat{Z}\hat{Z}} = 0. \tag{8}$$

Combining this with the condition of a fixed lower surface gives a uniform vertical deformation field $\hat{w} = -\hat{w}_s(1 + \hat{Z})$, where $\hat{w}_s = w_s/h$ is the normalized indentation displacement. We then exploit the surface traction $\mathbf{e}_3 \cdot \mathbf{P} \cdot \mathbf{e}_3|_{Z=0} = -p$ to obtain the pressure-displacement relation:

$$p = -\left.\frac{\mathrm{d}\Phi^{(0)}}{\mathrm{d}\hat{w}_{\hat{Z}}}\right|_{\hat{w}_{\hat{Z}}=-\hat{w}_s}, \tag{9}$$

which gives rise to a nonlinear Winkler-type response [15].

Specifically, for isotropic hyperelastic materials, for instance, the strain-energy function $\Phi(\mathcal{I}_1, \mathcal{I}_2, \mathcal{I}_3)$ can be expressed in terms of the three principal invariants of the right Cauchy-Green tensor $\mathbf{C} = \mathbf{F}^{\mathsf{T}} \cdot \mathbf{F}$. Their leading-order expressions can be readily calculated using Eq. (6)

$$\begin{aligned} \mathcal{I}_1^{(0)}(\hat{w}_{\hat{Z}}) &= 3 + 2\hat{w}_{\hat{Z}} + \hat{w}_{\hat{Z}}^2, \\ \mathcal{I}_2^{(0)}(\hat{w}_{\hat{Z}}) &= 3 + 4\hat{w}_{\hat{Z}} + 2\hat{w}_{\hat{Z}}^2, \\ \mathcal{I}_3^{(0)}(\hat{w}_{\hat{Z}}) &= 1 + 2\hat{w}_{\hat{Z}} + \hat{w}_{\hat{Z}}^2, \end{aligned} \tag{10}$$

so that $\Phi^{(0)}(\hat{w}_{\hat{Z}}) = \Phi(\mathcal{I}_i = \mathcal{I}_i^{(0)})$, where $i = 1, 2, 3$. More specifically, for the compressible neo-Hookean material in Eq. (2), the pressure-displacement relation simply reads

$$p = \left[\frac{2(1+\nu)}{3(1-2\nu)} + \frac{2(2-\hat{w}_s)}{3(1-\hat{w}_s)^{5/3}}\right] G\hat{w}_s \tag{11}$$

and reduces to the linear Winkler model [Eq. (4)] in the limit $|\hat{w}_s| \ll 1$, as shown in Fig. 2(b).

A salient feature of the nonlinear model in Eq. (11) is its singularity as $\hat{w}_s \to 1$ (i.e., full compression) due to the term $(1 - \hat{w}_s)^{-5/3}$. Interestingly, this behavior is reminiscent of a monatomic ideal gas undergoing adiabatic compression, for which the adiabatic index is $\gamma = 5/3$ and the relation $pV^\gamma = \text{const}$ holds. For a gas spring (or pneumatic chamber) with an (effective) initial pressure p_0, the gas volume varies as $V = V_0(1 - \hat{w}_s)$, leading to a pressure increase $\Delta p = p_0(V_0/V)^\gamma - p_0 = p_0[(1 - \hat{w}_s)^{-\gamma} - 1]$. Note that the exponent γ for a monatomic ideal gas is thermodynamic in origin, and its similarity to the present elastic problem lies only in the common power-law dependence of the free-energy contribution on volume change. We then introduce a mechanical system that combines an elastic spring and a gas spring in parallel to reproduce the nonlinear model, as shown in Fig. 2(a). Specifically, we set the initial pressure of the gas spring by matching the singular behavior as $\hat{w}_s \to 1$ and then choose the stiffness of the elastic spring by matching the small-deformation limit of Eq. (11) as $\hat{w}_s \to 0$. This yields

$$p \approx \frac{2(4+\nu)}{9(1-2\nu)} G\hat{w}_s + \frac{2}{3}G\left((1 - \hat{w}_s)^{-5/3} - 1\right), \tag{12}$$

which reproduces the compression hardening and tension softening of the neo-Hookean layer in Eq. (11) with an error within 2% for $|\hat{w}_s| < 1$ [Fig. 2(b)].

To compute the indentation force for a prescribed indentation depth $\hat{\delta} = \delta/h$, we integrate the normal pressure over the contact area. By changing the integration variable from $r\mathrm{d}r$ to $Rh\mathrm{d}\hat{w}_{\hat{z}}$ according to Eq. (1), with the integration domain mapped to $[-\hat{\delta}, 0]$, we obtain a simple relation

$$F = 2\pi Rh\Phi\left(\mathcal{I}_1^{(0)}, \mathcal{I}_2^{(0)}, \mathcal{I}_3^{(0)}\right)\Big|_{\hat{w}_{\hat{z}}=-\hat{\delta}}. \tag{13}$$

This shows that the full 3D nonlinear problem has reduced to a simple algebraic relation between F and $\hat{\delta}$, via exploiting axisymmetry, slenderness, and the spherical geometry of the indenter. For example, for neo-Hookean materials described by Eq. (2), we have

$$F = 2\pi GRh\left[\frac{(1+\nu)\hat{\delta}^2}{3(1-2\nu)} + \frac{3-2\hat{\delta}+\hat{\delta}^2}{2(1-\hat{\delta})^{2/3}} - \frac{3}{2}\right], \tag{14}$$

which agrees closely with the numerical results in Fig. 2(c) even as δ/h approaches 1. Equation (14) is derived under the thin-film assumption $\epsilon \ll 1$ and therefore does not recover the Hertz regime, which belongs to the opposite limit $\epsilon \gg 1$.

The simple form of Eq. (13) enables a convenient investigation of the indentation response of thin films with different constitutive laws. We consider neo-Hookean (N-H), Mooney-Rivlin (M-R), and Arruda-Boyce (A-B) hyperelastic models, choosing material parameters so that all reduce to the same small-strain elastic properties (G, ν) (see Section I.B in [15]). As shown in Fig. 3, the predictions of Eq. (13) exhibit excellent agreement with the corresponding FEM results. Notably, thin films governed by these three constitutive laws show identical responses at shallow indentation, as expected, and all display compression hardening at larger indentation depths.

A direct implication for interpreting indentation experiments is that any of these constitutive relations may be used to fit experimental data via Eq. (13): they all recover the same linear elastic properties, provided a good fit is obtained. Moreover, fitting data at large indentation depths can yield additional insight into the strain-stiffening behavior of the thin film. We therefore anticipate that, with this framework, the previously overlooked deep-indentation regime might serve as a standardized protocol for characterizing soft thin films such as biological cells, for which reported mechanical properties using Hertz-type theory and other methods (e.g., for breast cancer cells) can vary by up to three orders of magnitude across different studies [21,22]. In particular, the high compliance of living cells can make the contact point indistinct in the indentation curve [12]. Reducing its associated uncertainty typically

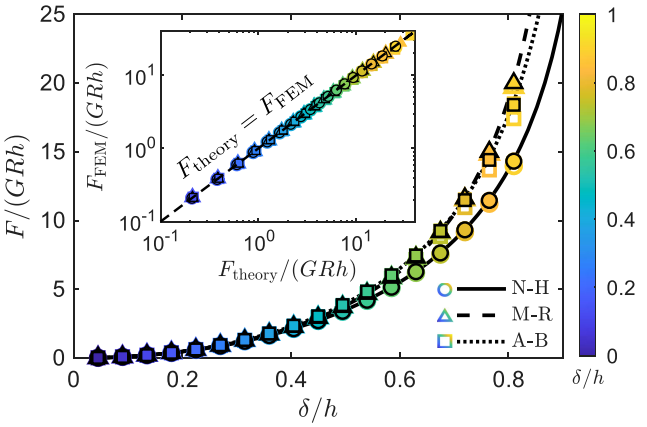

FIG. 3. Comparison between the leading-order theoretical prediction (curves, given by Eq. (13) and numerical results (markers) for different material models. We consider neo-Hookean (N-H, solid curves, circle markers), Mooney-Rivlin (M-R, dashed curves, triangle markers), and Arruda-Boyce (A-B, dotted curves, square markers) materials, all calibrated to share the same small-strain elastic properties. The indentation depth is encoded by the color bar; empty markers, filled markers with black edges, and fully colored markers correspond to numerics using $R/h = 10$, 10^2, and 10^3, respectively.

requires indentation depths of at least 400 nm, which are already comparable to the thickness of many cells [23]. Deep indentation is therefore not merely more experimentally accessible than shallow indentation but also a regime in which reliable interpretation becomes possible [5,8,10,24].

It is worth noting that the leading-order analysis does not apply to (nearly) incompressible materials ($\nu \to 0.5$), since Eq. (11) predicts a divergent stiffness in this limit. However, this singularity should not be interpreted as a physical singularity, but rather as an indication that the relevant asymptotic regime has changed. Extending the model to incompressible materials requires an $\mathcal{O}(\epsilon^2)$ analysis, in which the through-thickness deformation becomes nonuniform. In Section II.C of [15], we carry out this higher-order analysis and obtain a nonlinear, nonlocal pressure–displacement relation. We further show that the extended model provides good agreement with FEM results in the (nearly) incompressible regime. In addition, the analysis motivates an incompressibility parameter $\mathcal{C} = 2(1+\nu)h/[3(1-2\nu)R]$, which quantifies the importance of the correction: when $\mathcal{C} \gtrsim 1$, the second-order term becomes significant. Nevertheless, for slender configurations with $R \gg h$, the leading-order (compressible) model is not that restrictive, as $\mathcal{C} \ll 1$ is readily satisfied as long as ν is not too close to $1/2$.

Finally, we discuss the reverse process in which the indenter is pulled away after a deep indentation has been performed. In practical settings—such as in cell films [6,12]—adhesive interactions between the indenter and the film often develop during indentation. A salient feature

of this interaction is the appearance of a finite force required to detach the sphere from the film, known as the pull-off force [25,26]. This pull-off force can provide quantitative insight into cell-cell adhesion or the adhesion of cell-therapy particles [27–29]. This raises an immediate question: how do different material laws influence the magnitude of the pull-off force?

The key to addressing this question lies in determining the condition at the contact line $r = a$. In the absence of adhesion, we assumed that the contact pressure vanishes at the edge, so that the mapped integration domain used to derive Eq. (13) is simply $[-\hat{\delta}, 0]$. In the presence of adhesion, however, the contact pressure becomes negative, allowing the sphere to pull the thin film upward by a displacement $\hat{\delta}_c = \delta_c/h$ [Fig. 4(a)]. We note that the leading-order analysis predicts a displacement discontinuity at $r = a$, as sketched in Fig. 4(a). The associated error is $\mathcal{O}(\epsilon)$ (Fig. S4 [15]). An infinitesimal crack advance of width Δr requires an energy cost of $2\pi a \Delta r \Gamma$ to create new surfaces, while releasing elastic energy $2\pi a \Delta r \Phi^{(0)}(\hat{w}_{\hat{Z}} = \hat{\delta}_c)$ due to the reduction of the deformed area, where Γ is the adhesion energy per unit area. Balancing the two gives the fracture criterion $\Phi^{(0)}(\hat{\delta}_c) = \Gamma/h$.

Therefore, to incorporate adhesion, the mapped integration domain simply changes to $[-\hat{\delta}, \hat{\delta}_c = (\Phi^{(0)})^{-1}(\Gamma/h)]$,

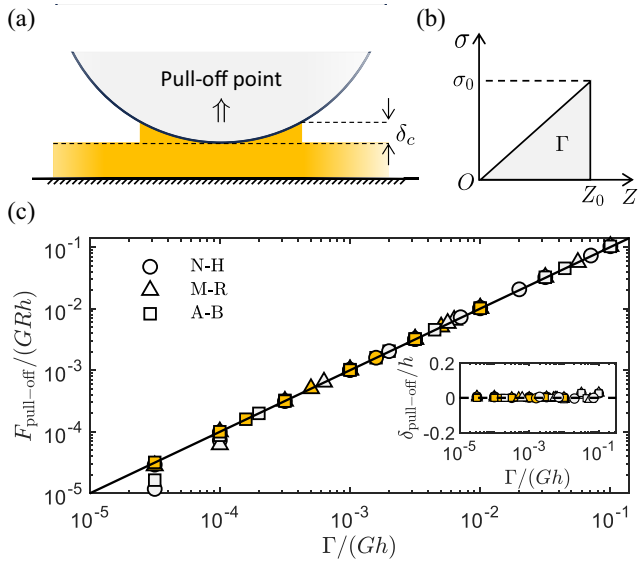

FIG. 4. (a) Schematic of the geometry at the pull-off point in the presence of interfacial adhesion. (b) Bi-linear cohesive model used to simulate adhesion with a maximum stress σ_0 at the separation distance Z_0. The area under the curve corresponds to the adhesion energy Γ. (c) Pull-off force and pull-off displacement as functions of the adhesion energy Γ. Simulations with two different microstiffness values, $\sigma_0 h/(GZ_0) = 0.1$ (gray markers) and 1.0 (yellow markers), demonstrate numerical convergence. Data from all three constitutive models collapse onto the master curve given by Eq. (17) for the pull-off force and Eq. (16) for the pull-off displacement (shown in the inset).

yielding

$$F = 2\pi R h \left[\Phi^{(0)}(-\hat{\delta}) - \Gamma/h\right]. \tag{15}$$

Since the strain-energy function is positive definite, the pull-off force corresponds to the maximum value of $-F$ during withdrawal, which occurs at

$$\hat{\delta}_{\text{pull-off}} = 0, \tag{16}$$

giving

$$F_{\text{pull-off}} = 2\pi R \Gamma, \tag{17}$$

which is strikingly independent of the constitutive law of the film. This result is also consistent with the prediction based on linear elasticity and small deformations [17].

To validate this universal pull-off prediction, we perform FEM simulations using a cohesive-zone model to represent adhesion [see Fig. 4(b)] [30]. At the microscopic level, the cohesive traction increases with the local separation between the two surfaces, reaching a peak value σ_0 at a characteristic separation Z_0, beyond which the traction rapidly decays to zero. The area under this traction-separation curve corresponds to the macroscopic adhesion energy Γ. Thus, once Γ is specified, a single additional parameter determines the cohesive behavior; here we take it to be the nondimensional ratio $\sigma_0 h/(GZ_0)$. In the numerical simulations, we test two representative values, $\sigma_0 h/(GZ_0) = 0.1$ (gray markers) and 1.0 (yellow markers), as shown in Fig. 4(c). Our theoretical predictions for both the pull-off displacement in Eq. (16) (dashed line in the inset of Fig. 4) and the pull-off force in Eq. (17) (solid line in Fig. 4) show excellent agreement with the numerical results across a broad range of adhesion energies and for all three constitutive laws considered. Such a constitutive-law-independent relation provides a foundation for characterizing adhesion in thin-film systems of diverse material behaviors [31].

Acknowledgments—This work was supported by the National Natural Science Foundation of China (Grant No. 12372103, 12432003). Z. D. acknowledges the support of the Peking Nanofab. The authors thank J. Li for the useful discussion on FEM simulations.

Data availability—The data that support the findings of this article are openly available from GitHub [32].

[1] D. Vella, A. Ajdari, A. Vaziri, and A. Boudaoud, Indentation of ellipsoidal and cylindrical elastic shells, Phys. Rev. Lett. **109**, 144302 (2012).

[2] D. Vella, J. Huang, N. Menon, T. P. Russell, and B. Davidovitch, Indentation of ultrathin elastic films and the

emergence of asymptotic isometry, Phys. Rev. Lett. **114**, 014301 (2015).
[3] D. Vella and B. Davidovitch, Indentation metrology of clamped, ultra-thin elastic sheets, Soft Matter **13**, 2264 (2017).
[4] S. Zhao and P. A. Haas, Mechanics of poking a cyst, Phys. Rev. Lett. **134**, 228402 (2025).
[5] K. Geng, F. Yang, T. Druffel, and E. A. Grulke, Nanoindentation behavior of ultrathin polymeric films, Polymer **46**, 11768 (2005).
[6] A. Viljoen, M. Mathelié-Guinlet, A. Ray, N. Strohmeyer, Y. J. Oh, P. Hinterdorfer, D. J. Müller, D. Alsteens, and Y. F. Dufrêne, Force spectroscopy of single cells using atomic force microscopy, Nat. Rev. Methods Primers **1**, 63 (2021).
[7] M. Lekka and P. Laidler, Applicability of AFM in cancer detection, Nat. Nanotechnol. **4**, 72 (2009).
[8] S. Zak, C. Trost, P. Kreiml, and M. Cordill, Accurate measurement of thin film mechanical properties using nanoindentation, J. Mater. Res. **37**, 1373 (2022).
[9] E. K. Dimitriadis, F. Horkay, J. Maresca, B. Kachar, and R. S. Chadwick, Determination of elastic moduli of thin layers of soft material using the atomic force microscope, Biophys. J. **82**, 2798 (2002).
[10] N. Gavara and R. S. Chadwick, Determination of the elastic moduli of thin samples and adherent cells using conical atomic force microscope tips, Nat. Nanotechnol. **7**, 733 (2012).
[11] K. L. Johnson, *Contact Mechanics* (Cambridge University Press, Cambridge, England, 1987), p. 140.
[12] M. Krieg, G. Fläschner, D. Alsteens, B. M. Gaub, W. H. Roos, G. J. Wuite, H. E. Gaub, C. Gerber, Y. F. Dufrêne, and D. J. Müller, Atomic force microscopy-based mechanobiology, Nat. Rev. Phys. **1**, 41 (2019).
[13] Z. Dai, Jump of an atomic force microscopy probe towards an elastic substrate in a liquid environment, J. Fluid Mech. **1013**, A49 (2025).
[14] O. Gonzalez and A. M. Stuart, *A First Course in Continuum Mechanics* (Cambridge University Press, Cambridge, England, 2008), Vol. 42, p. 287.
[15] See Supplemental Material at http://link.aps.org/supplemental/10.1103/8s5j-63xf for details of numerical methods, nonlocal incompressible models appearing at higher orders, and supporting numerical results, which includes Refs. [12,14,16,17].
[16] T. G. Chandler and D. Vella, Validity of Winkler's mattress model for thin elastomeric layers: Beyond Poisson's ratio, Proc. R. Soc. A **476**, 20200551 (2020).
[17] F. Yang, Asymptotic solution to axisymmetric indentation of a compressible elastic thin film, Thin Solid Films **515**, 2274 (2006).
[18] J. R. Barber, *Contact Mechanics* (Springer, New York, 2018), Vol. 20, Chap. 14.2.
[19] M. Jaffar, Asymptotic behaviour of thin elastic layers bonded and unbonded to a rigid foundation, Int. J. Mech. Sci. **31**, 229 (1989).
[20] P. Howell, G. Kozyreff, and J. Ockendon, *Applied Solid Mechanics* (Cambridge University Press, Cambridge, England, 2009), p. 43, Chap. 6.
[21] C. F. Guimarães, L. Gasperini, A. P. Marques, and R. L. Reis, The stiffness of living tissues and its implications for tissue engineering, Nat. Rev. Mater. **5**, 351 (2020).
[22] P.-H. Wu, D. R.-B. Aroush, A. Asnacios, W.-C. Chen, M. E. Dokukin, B. L. Doss, P. Durand-Smet, A. Ekpenyong, J. Guck, N. V. Guz *et al.*, A comparison of methods to assess cell mechanical properties, Nat. Methods **15**, 491 (2018).
[23] A. Rigato, A. Miyagi, S. Scheuring, and F. Rico, High-frequency microrheology reveals cytoskeleton dynamics in living cells, Nat. Phys. **13**, 771 (2017).
[24] S. Yang, Y. Liu, Y. Su, H. Gao, K. Sun, Q. Xu, Q. Zhang, and Y. Xu, Three-dimensional imaging and measurement of the microscale deformation in soft thin films under micro-indentation, Extreme Mech. Lett. **78**, 102355 (2025).
[25] K. L. Johnson, K. Kendall, and A. Roberts, Surface energy and the contact of elastic solids, Proc. R. Soc. A **324**, 301 (1971).
[26] M. Ciavarella, J. Joe, A. Papangelo, and J. Barber, The role of adhesion in contact mechanics, J. R. Soc. Interface **16**, 20180738 (2019).
[27] C. Yu, W. Zeng, B. Wang, X. Cui, Z. Gao, J. Yin, L. Liu, X. Wei, Y. Wei, and Z. Dai, Stiffer is stickier: Adhesion in elastic nanofilms, Nano Lett. **25**, 1876 (2024).
[28] K. Haase and A. E. Pelling, Investigating cell mechanics with atomic force microscopy, J. R. Soc. Interface **12**, 20140970 (2015).
[29] J. Hu, S. Youssefian, J. Obayemi, K. Malatesta, N. Rahbar, and W. Soboyejo, Investigation of adhesive interactions in the specific targeting of triptorelin-conjugated PEG-coated magnetite nanoparticles to breast cancer cells, Acta Biomater. **71**, 363 (2018).
[30] X.-P. Xu and A. Needleman, Numerical simulations of fast crack growth in brittle solids, J. Mech. Phys. Solids **42**, 1397 (1994).
[31] W. Zheng and Z. Dai, Universal pull-off force for separating a rigid sphere from a membrane, J. Mech. Phys. Solids, 106163 (2025).
[32] https://github.com/ZhaoheDai/2026_PRL.